pressure affects the phonon spectrum essentially by increasing all phonon frequencies, we can explain the decrease in T_c observed in many superconductors on compression, as has been done recently for MgB_2 (*10, 29*).

That T_c in boron increases substantially with pressure may be due to one of the following: (i) The factor $\eta = N(0)\langle I^2\rangle$ may increase with pressure in B, thus suppressing the effect of increasing $\langle\omega^2\rangle$. The Hopfield parameter, η, may also contribute to the increase in T_c if the character of the conduction electrons also changes under pressure, as in *s-d* transfer. (ii) The $\langle\omega^2\rangle$ factor may actually decrease with pressure if the phonon modes responsible for electron-phonon coupling soften under pressure. (iii) The parameter μ^* decreases on compression, which would be related to pressure-induced additional screening of the electron-electron interaction. Of these, the first and third options are possibilities: Both may be effective if B is approaching a covalent instability (with η increasing), as discussed by Allen and Dynes (*30*); or it transforms to a compensated metal, as in the cases discussed by Richardson and Ashcroft (*31*). A similar increase in critical temperature ($dT_c/dP \approx 0.05$ K/GPa) is observed in metallic S after transforming to the β-Po structure at 160 GPa (*32*), suggesting that the mechanism could be related.

We have found superconductivity in B at pressures above 160 GPa. The pressure of metallization is in the general range of (but somewhat lower than) theory, which predicted that the transition would be accompanied by the loss of covalent bonding to form a dense nonicosahedral structure (*12*). The magnitude of T_c appears to be consistent with such a transition and with an electron-coupling origin for the superconductivity. This work extends the range of electrical conductivity measurements to a record value of 250 GPa. These observations should stimulate theoretical calculations of superconductivity in elemental B and related low-*Z* substances.

References and Notes

1. J. Bardeen, L. N. Cooper, J. R. Schrieffer, *Phys. Rev.* **108**, 1175 (1957).
2. N. W. Ashcroft, *Phys. Rev. Lett.* **21**, 1748 (1968); C. F. Richardson, N. W. Ashcroft, *Phys. Rev. Lett.* **78**, 118 (1997).
3. D. A. Papaconstantopoulos *et al*., *Phys. Rev. B* **15**, 4221 (1977).
4. K. A. Johnson, N. W. Ashcroft, *Nature* **403**, 632 (2000); M. Städele, R. M. Martin, *Phys. Rev. Lett.* **84**, 6070 (2000).
5. K. M. Lang *et al*., *J. Low Temp. Phys.* **114**, 445 (1999).
6. N. E. Christensen, D. L. Novikov, *Phys. Rev. Lett.* **86**, 1861 (2001); J. B. Neaton, N. W. Ashcroft, *Nature* **400**, 141 (1999).
7. K. Takei, K. Nakamura, Y. Maeda, *J. Appl. Phys.* **57**, 5093 (1985); V. I. Tutov, E. E. Semenenko, *Sov. J. Low Temp. Phys.* **16**, 22 (1990).
8. R. J. Cava *et al.*, *Nature* **367**, 146 (1994); *Nature* **367**, 252 (1994).
9. J. Nagamatsu, N. Nakagawa, T. Muranaka, Y. Zenitani, J. Akimitsu, *Nature* **410**, 63 (2001).
10. M. Monteverde *et al.*, *Science* **292**, 75 (2001); T. Tomita, J. J. Hamlin, J. S. Schilling, D. G. Hinks, J. D. Jorgensen, preprint available at http://xxx.lanl.gov/abs/cond-mat/0103538; B. Lorenz, R. L. Meng, C. W. Chu, *Phys. Rev. B* **64**, 12507 (2001); V. G. Tissen *et al.*, preprint available at http://xxx.lanl.gov/abs/cond-mat/0105475; V. V. Struzhkin *et al.*, prerpint available at http://xxx.lanl.gov/abs/cond-mat/0106576, and references therein.
11. J. Kortus, I. I. Mazin, K. D. Belashchenko, V. P. Antropov, L. L. Boyer, *Phys. Rev. Lett.* **86**, 4656 (2001).
12. C. Mailhiot, J. B. Grant, A. K. McMahan, *Phys. Rev. B* **42**, 9033 (1990).
13. D. A. Young, *Phase Diagrams of the Elements* (Univ. of California Press, Berkeley, CA, 1991).
14. N. Vast *et al*., *Phys. Rev. Lett.* **78**, 693 (1997).
15. M. Fujimori *et al*., *Phys. Rev. Lett.* **82**, 4452 (1999).
16. Y. Ma *et al.*, *Trans. Am. Geophys. Union* **81**, S39 (2000).
17. M. I. Eremets, K. Shimizu, T. C. Kobayashi, K. Amaya, *Science* **281**, 1333 (1998).
18. M. I. Eremets *et al*., *Phys. Rev. Lett.* **85**, 2797 (2000).
19. H. K. Mao, J. Xu, P. M. Bell, *J. Geophys. Res.* **91**, 4673 (1986).
20. O. Madelung, M. Schultz, H. Weiss, Eds., *Landolt-Börnstein. New Series*, vol. 17e (Springer-Verlag, Berlin, 1983).
21. M. I. Eremets, *High Pressure Experimental Methods* (Oxford Univ. Press, Oxford, 1996).
22. The superconducting step cannot be attributed to Pt or Pd electrical wires in series with the sample, because the same superconducting transitions were observed for both electrodes. In addition, we proved that the Pt electrodes did not reveal a superconducting transition on cooling down to 50 mK in previous experiments on CsI up to 220 GPa (*17*). In those experiments, the only superconducting transition was that of the CsI sample, which appeared at 1.6 K and 203 GPa and shifted to lower temperatures with pressure. We also did not observe any superconductivity in experiments on Xe to 155 GPa and 27 mK, using the same arrangement of Pt electrodes (*18*). Only recently has superconductivity been found in compacted Pt powder, but at very low temperatures; i.e., $T_c < 1.38$ mK [R. König, A. Schindler, T. Herrmannsdörfer, *Phys. Rev. Lett.* **82**, 4528 (1999)]. We note that the BN/epoxy layer is also in contact with the sample and electrodes. However, this mixture remains insulating to at least 240 GPa, as demonstrated by recent experiments on N [M. I. Eremets *et al*., *Nature* **411**, 170 (2001)], and consistent with the experiments described above. Thus, although the Meissner effect was not examined (*17*), the resistance steps measured here can be attributed to superconductivity in the B samples.
23. The initial pressure derivative is very large (~0.2 K/GPa). Extrapolation of this line to lower pressure gives $T_c = 0$ K at ~130 GPa, which correlates with a kink in the room-temperature *R(P)* curve. This suggests the possibility that the transition to the metallic state occurs at ~130 GPa, whereas the change near 180 GPa arises from a phase transition.
24. N. F. Mott, *Metal-Insulator Transitions* (Taylor & Francis, London, ed. 2, 1990).
25. We note that bct and face-centered tetragonal (fct) share the same Bravais lattice. Hence, a transition from bct to fcc is structurally similar to moving from In to Al within the group IIIA family. The latter is accompanied by an increase in zero-pressure T_c by a factor of three [N. W. Ashcroft, N. D. Mermin, *Solid State Physics* (Harcourt, New York, 1976)].
26. The modes in α-B extend to 1300 cm^{-1} at high pressure (*13*). The frequency of diatomic B is ~1000 cm^{-1} [K. P. Huber, G. Herzberg, *Constants of Diatomic Molecules* (Van Nostrand, New York, 1979)].
27. D. U. Gubser, A. W. Webb, *Phys. Rev. Lett.* **35**, 104 (1975); M. M. Dacorogna, M. L. Cohen, P. K. Lam, *Phys. Rev. B* **34**, 4865 (1986).
28. W. L. McMillan, *Phys. Rev.* **167**, 331 (1968).
29. I. Loa, K. Syassen, *Solid State Commun.* **118**, 279 (2001); T. Vogt, G. Schneider, J. A. Hriljac, G. Yang, J. S. Abell, *Phys. Rev. B.* **63**, 220505 (2001); A. F. Goncharov *et al.*, preprint available at http://xxx.lanl.gov/abs/cond-mat/0104042.
30. P. B. Allen, R. C. Dynes, *Phys. Rev. B* **12** (1975).
31. C. F. Richardson, N. W. Ashcroft, *Phys. Rev. B* **55**, 15130 (1997).
32. V. V. Struzhkin, R. J. Hemley, H. K. Mao, Y. A. Timofeev, *Nature* **390**, 382 (1997).

33. We are grateful to N. W. Ashcroft for useful discussions and S. Gramsch for comments on the manuscript. Supported by NSF.

4 May 2001; accepted 30 May 2001

Observation of Chaos-Assisted Tunneling Between Islands of Stability

Daniel A. Steck, Windell H. Oskay, Mark G. Raizen*

We report the direct observation of quantum dynamical tunneling of atoms between separated momentum regions in phase space. We study how the tunneling oscillations are affected as a quantum symmetry is broken and as the initial atomic state is changed. We also provide evidence that the tunneling rate is greatly enhanced by the presence of chaos in the classical dynamics. This tunneling phenomenon represents a dramatic manifestation of underlying classical chaos in a quantum system.

Quantum-mechanical systems can display very different behavior from their classical counterparts. In particular, quantum effects suppress classical chaotic behavior, where simple deterministic systems exhibit complicated and seemingly random dynamics (*1*). Nevertheless, aspects of quantum behavior can often be understood in terms of the presence or absence of chaos in the classical limit. In this report, we focus on quantum transport in a mixed system, where the classical dynamics are complicated by the coexistence of chaotic and stable behavior. We study quantum tunneling between two stable regions (referred to as nonlinear resonances or islands of stability) in the classical phase space. The classical transport between these islands is

Department of Physics, The University of Texas at Austin, Austin, TX 78712–1081, USA.

*To whom correspondence should be addressed. E-mail: raizen@physics.utexas.edu

forbidden by dynamical "barriers" in phase space. In contrast, quantum tunneling can couple the two islands so that a wave packet oscillates coherently between the two symmetry-related stable regions (*2*–*14*).

"Dynamical tunneling," where the classical transport is forbidden because of the system dynamics and not a potential barrier, was originally introduced in the context of a two-dimensional, time-independent potential (*2*). Subsequently, it was found that the presence of chaos could markedly enhance the tunneling rate in a driven, double-well potential (*3*), and the role of a discrete symmetry in this system was highlighted in the tunneling process (*4*). In addition to symmetry, the presence of regular islands is important for producing coherent tunneling, because the islands cause localization of the Floquet states (*5*), which are the analogs of energy eigenstates in time-periodic quantum systems (*1*). Thus, dynamical tunneling between islands of stability is analogous to tunneling in the simple double-well potential, where the localized eigenstates split into a symmetric/antisymmetric pair, and the tunneling can be understood in terms of the dephasing of this nearly degenerate Floquet-state doublet. It was found that the tunneling rate is correlated with the degree of overlap of the tunneling states with the chaotic region, again pointing to the role of the chaotic sea in assisting the tunneling transport (*6*). The possible enhancement of the tunneling rate because of the presence of the chaotic region was understood in terms of a three-level process, where the tunneling doublet interacts with a third state associated with the chaotic region. The term "chaos-assisted tunneling" was introduced (*7*, *8*) to distinguish this process from ordinary dynamical tunneling, which is a two-state process. Chaos-assisted tunneling has also been explained in terms of indirect paths, which are multiple-step transitions that traverse the chaotic region, as opposed to direct paths, which tunnel in a single step and are responsible for regular dynamical tunneling (*9*). Because of these coexisting direct and indirect mechanisms, the presence of the chaotic region produces large fluctuations in the tunneling rate as the system parameters vary, sometimes increasing the tunneling rate by orders of magnitude.

Previous experimental work on dynamical and chaos-assisted tunneling has mainly focused on wave analogies to these effects. Chaos-assisted tunneling has been studied in microwave billiards, where the enhancement of mode doublet splittings due to classical chaos has been detected spectroscopically (*15*). The Shnirelman peak in the level spacing distribution is a similar statistical signature of dynamical tunneling (*16*) and has been observed in acoustic resonator (*17*) and microwave cavity experiments (*18*). Finally, another recent atom-optics experiment has examined coherent tunneling in a double-well optical lattice potential (*19*, *20*).

Our experiment studies the motion of cold cesium atoms in an amplitude-modulated standing wave of light. Because the light is detuned far from the D_2 line (50 GHz, or 10^4 natural linewidths, to the red of the $F = 3 \rightarrow F'$ transition, where F is the atomic hyperfine quantum number), the internal dynamics of the atom can be adiabatically eliminated (*21*, *22*). The atomic center-of-mass Hamiltonian can then be written in scaled units as

$$H = p^2/2 - 2\alpha\cos^2(\pi t)\cos(x) \qquad (1)$$

where x and p are the canonical position and momentum coordinates, respectively, t is time, and α is given by $(8\omega_r T^2/\hbar)\ V_0$ [V_0 is the amplitude of the ac Stark shift corresponding to the time-averaged laser intensity, T is the period of the temporal modulation, $\hbar$ is the reduced Planck constant, and ω_r is the recoil frequency, which has the numerical value $2\pi \times 2.07$ kHz for this experiment); more details on the unit scaling can be found in (*22*). The quantum description of this system is governed by one additional parameter, the effective Planck constant $\bar{\hbar} = 8\omega_r T$, so that the scaled coordinate operators satisfy $[x, p] = i\bar{\hbar}$ (note, however, that for the experimental data we report momentum in units of double photon recoils, $2\hbar k_L$, which is equivalent to the scaled momentum expressed in multiples of $\bar{\hbar}$). The time-dependent potential in this system can be decomposed into a sum of three unmodulated cosine terms (*23*). One of these terms is stationary, whereas the other two move with velocity $\pm 2\pi$, so that in the limit of vanishing α, the phase space of this system has three primary resonances, two of which are symmetric partners about the $p = 0$ axis. The value of α used in the experiment was $10.5 \pm 5\%$. At this large value of α, the central island has mostly vanished, leaving a large chaotic region surrounding the two symmetry-related islands (Fig. 1, A and B). To study chaos-assisted tunneling, we prepared the atoms in one of the resonances and observed the atoms coherently oscillate between the two islands by monitoring the evolution of the atomic momentum distribution. The possibility of experimentally observing chaos-assisted tunneling in this system has been a subject of recent discussion (*10*–*12*), and the tunneling and band structure in this system were recently treated in an extensive numerical study (*10*).

The basic experimental apparatus has been described in detail in (*22*), although we have made several major improvements, as we now describe. To prepare the initial atomic state, we first cooled and trapped 10^6 cesium atoms from the background vapor in a standard six-beam magneto-optic trap (MOT), at a temperature of 10 μK (corresponding to a Gaussian momentum distribution with $\sigma_p/\hbar k_L = 4$). The atoms are then further cooled and stored for 300 ms in a three-dimensional, far detuned, linearly polarized optical lattice similar to that of (*24*). After adiabatic release from the lattice, the atoms achieve a temperature of 400 nK ($\sigma_p/\hbar k_L = 1.4$). The atoms are then optically pumped to the $F = 4$, $m = 0$ magnetic sublevel, resulting in a temperature of 3 μK ($\sigma_p/\hbar k_L = 4$). The atomic orientation is maintained with a 1.5-G bias field. A velocity-selective, stimulated Raman pulse on the 9.2-GHz clock transition (which is insensitive to Zeeman shifts to first order) "tags" a narrow velocity slice (of less than 1% of the atoms) into the $F = 3$, $m = 0$ sublevel near $p = 0$. The Raman fields are generated with a setup similar to that in (*25*), and the 800-μs square temporal pulse yields a momentum slice with a half-width at half-maximum of $0.03 \times 2\hbar k_L$. The remaining atoms are then removed by applying low-intensity, circularly polarized light resonant on the $F = 4 \rightarrow F' = 5$ cycling transition for 800 μs.

At this point, the atoms have been prepared in a very narrow distribution about $p = 0$, but they are not localized in position on the scale of the standing-wave period. A one-dimensional optical lattice is ramped on adiabatically so that the atoms localize in the potential wells. The lattice is then suddenly spatially shifted by 1/4 of the lattice period (in several hundred ns) with an electrooptic modulator placed before the standing-wave retroreflector. After 6 μs of evolution in the lattice, the atoms return to the centers of the potential wells, acquiring kinetic energy in the meantime. The resulting Gaussian momentum profile is peaked at $4.1 \times 2\hbar k_L$, with a width $\sigma_p = 1.1 \times 2\hbar k_L$. This state preparation procedure produces a localized atomic wave packet centered on one of the islands of stability (Fig. 1, A and B). The three red ellipses are the 50% contours of a classical distribution with the same position and momentum marginal distributions as the Wigner function. (The Wigner function has additional structures that reflect the coherences of the initial state.) The initial condition shown does not reflect a slight distortion due to anharmonic motion in the lattice. The importance of the extremely narrow velocity selection is twofold. First, the atomic distribution must be selected to be well within one photon recoil of zero momentum, so that all the atoms load into the lowest energy band of the lattice. Then, in the deep-well limit, the atomic distribution becomes minimum-uncertainty Gaussian (modulo the standing-wave period). Second, only atoms whose momenta are nearly a multiple of $\hbar k_L$ will tunnel, as we discuss further below. As the lattice only imparts momentum in multiples of $2\hbar k_L$, the ramping and shifting of the lattice result in a

distribution with an overall Gaussian envelope but concentrated in narrow momentum slices around $n(2\hbar k_L)$ for integer n. This structure indicates coherence of the wave packet over multiple periods of the optical lattice.

After the state preparation, the atoms are subjected to the time-dependent interaction described by Eq. 1, with a modulation period of $T = 20$ μs ($\tilde{k} = 2.08$). The atoms are then allowed to expand freely for 20 ms, after which the optical molasses is turned on, freezing the atoms in place. The fluorescence of the atoms is collected on a charge-coupled device camera. As a result of the long free-drift time, this process yields a measurement of the atomic momentum distribution. Because of the relatively large size ($\sigma_x = 0.15$ mm) of the initial atomic cloud, the individual momentum slices are not resolved in the measured distributions. To compensate for the loss in signal that results from discarding most of the atoms, we averaged the data presented in this report over 20 iterations, except for the distributions in Fig. 1D (100 iterations) and Fig. 5A (19 iterations). The momentum distributions are sampled every two modulation periods (40 μs) for all the data presented here except for the high temporal resolution data (Fig. 5A).

The measured evolution of the momentum distribution (Fig. 1C) shows clear tunneling oscillations between the initial momentum peak and its symmetric partner, which is located $8 \times 2\hbar k_L$ away in momentum. Four damped oscillations are apparent in this measurement out to 80 modulation periods (1600 μs), and after this time the oscillations have completely damped away. Four of the momentum distributions near the beginning of the evolution are shown in more detail in Fig. 1D. During the first oscillation, nearly half of the atoms appear in the secondary peak (*26*).

As mentioned above, only atoms with momentum of approximately a multiple of a photon recoil momentum (or scaled momentum of nearly a multiple of $\tilde{k}/2$) will tunnel. This is clear from the requirement of symmetry for tunneling to occur, because only states that involve these special velocity classes are coupled to their symmetric reflections (about the $p = 0$ axis) by two-photon transitions. This is essentially the same condition required for Bragg scattering (*27*–*29*). The broken symmetry resulting from selecting other velocity classes is formally equivalent to a broken time-reversal symmetry (*30*) and suppresses the formation of symmetric/antisymmetric doublets (*30*, *31*). We can study this broken symmetry directly by varying the Raman detuning of the velocity-selection pulse from the optimum value and monitoring the effect on the evolution of the average momentum $\langle p \rangle$ (Fig. 2). The case with the strongest momentum oscillations corresponds to the data shown in Fig. 1, C and D. Also shown are measurements with Raman detunings corresponding to momentum offsets of $0.05 \times 2\hbar k_L$ and $0.12 \times 2\hbar k_L$. In the former case, the oscillations are partially suppressed, and for the larger detuning, the tunneling oscillations have mostly disappeared. Because of this sensitivity to the initial momentum, the tunneling oscillations are not visible without subrecoil velocity selection, as we have experimentally verified (*32*). Additionally, this effect is largely responsible for the damping of the tunneling oscillations that we observe, because the states near the edge of the Raman velocity selection profile will not tunnel as efficiently as the "resonant" states at the profile center. The various states will also tunnel at slightly different rates, leading to dephasing of the oscillations, similar to broadened excitation of a two-level system. Hence, narrower velocity selection should lead to longer damping times, although noise and decoherence sources may also limit the coherence of the oscillations.

We also verified that the tunneling is strongest if the wave packet is initially centered on the island of stability. As the initial wave packet is moving, we can displace the initial condition in the x direction in phase space simply by inserting a short delay time where the standing wave is off before beginning the driven pendulum interaction. The oscillations in $\langle p \rangle$ were compared for delay times of 0, 3.8, 7.6, and 15.1 μs, corresponding to displacements of 0, 1/4, 1/2, and 1 periods of the optical potential away from the island center (Fig. 3). For the 1/4-period displacement, the oscillations are suppressed, but still present. The initial wave packet in this case only weakly excites the tunneling Floquet states and mostly populates the states in the chaotic sea (resulting in diffusion throughout the sea) and states in the outer stability band (resulting in trapping of the

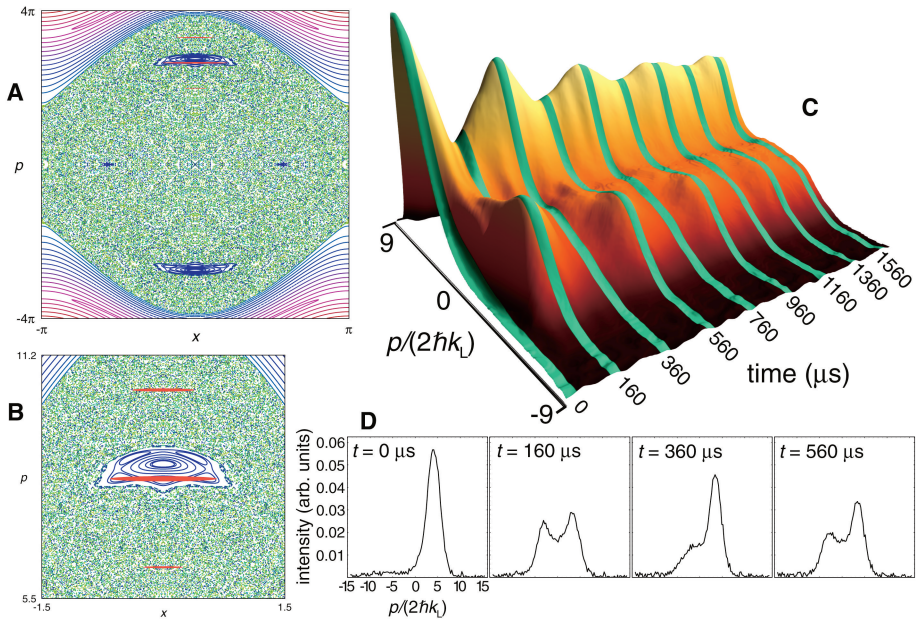

Fig. 1. Experimental observation of tunneling oscillations. (**A**) The classical phase space for the experimental parameters. The islands of stability involved in the tunneling appear as two blue regions inside the green chaotic region and are symmetric reflections about the $p = 0$ axis. A schematic of the initial atomic state is superimposed on the upper island in red, appearing as three narrow ellipses. (**B**) Magnified view of the upper stability island and the initial condition. (**C**) The measured evolution of the momentum distribution in time, showing several coherent oscillations between the two islands, which are separated in momentum by $8 \times 2\hbar k_L$. In this plot, the distribution is sampled every 40 μs (every two modulation periods). (**D**) Detailed view of the first four highlighted distributions in (C), where it is clear that a substantial fraction of the atoms tunnel to the other island (*2*).

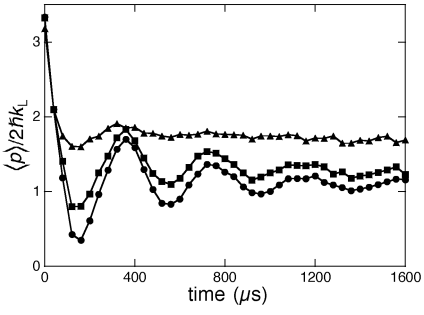

Fig. 2. Comparison of tunneling oscillations for different Raman detunings. The strongest oscillations observed (●) correspond to Raman velocity selection at $p = 0$. The other two cases are for velocity selection at $p = 0.05 \times 2\hbar k_L$ (■), where the oscillations are partially suppressed, and $p = 0.12 \times 2\hbar k_L$ (▲), where the oscillations are almost completely suppressed.

wave packet at the high momenta). For the 1/2-period displacement, the oscillations are completely suppressed, because the wave packet is almost entirely trapped in the outer stable region. For the longest delay, the wave packet returns to the island center, and the tunneling oscillations are once again present. The amplitude of the oscillations is somewhat suppressed in this case, however, because the free evolution stretches the wave packet, and hence the tunneling states are not as efficiently populated.

So far, we have discussed the tunneling oscillations and how they are affected by a broken quantum symmetry and the initial location in phase space, which are important characteristics of dynamical tunneling. To demonstrate chaos-assisted tunneling requires further evidence, and an important test is to compare the tunneling in the time-dependent potential with tunneling in the absence of chaos. A sensible integrable counterpart of the amplitude-modulated standing-wave system arises by simply considering the time-averaged potential, resulting in the quantum pendulum. Because the initial distribution is centered outside the separatrix, classical transport across the $p = 0$ axis is also forbidden in this system. However, there is a well-known dynamical tunneling mechanism in the pendulum, high-order Bragg scattering (*27–29*), which is a manifestation of quantum above-barrier reflection (*33*). As the wave packet is initially peaked near $4 \times 2\hbar k_L$, the dominant transport process is eighth-order Bragg scattering. For the parameters in the experiment, the calculated eighth-order Bragg period is around 1 s, which is much longer than the 400-μs tunneling period in the (chaotic) driven pendulum. We compared the evolution of $\langle p \rangle$ for the driven pendulum to the transport in the undriven pendulum (Fig. 4), and indeed no coherent oscillations are observed in the undriven case during the interaction times measured in the experiment. Hence, we observe that the classical chaos enhances the tunneling rate for these experimental parameters, in the sense that the tunneling in the presence of classical chaos occurs at a substantially greater rate than the tunneling in the integrable case.

Although it is customary to study time-periodic systems in a stroboscopic sense, sampling only at a particular phase of the modulation as we have done up to this point, it is also interesting to study the continuous tunneling dynamics in our system. We studied the evolution of the momentum distribution during the first half of the first tunneling period, sampling the system at 1-μs intervals, or 20 times per modulation period (Fig. 5A). The most obvious aspect of this data is that the initial and secondary (tunneled) peaks exhibit complementary but opposite momentum oscillations at the modulation frequency. These oscillations can be explained in terms of the continuous motion of the corresponding islands in phase space (Fig. 5B). As the two islands have opposite momentum, they move in opposite directions but oscillate in momentum because of repulsion by the remnants of the center island (*34*). In this picture, the islands constitute a pair of nonintersecting "flux tubes" (*14*) that remain confined in separated momentum intervals. The tunneling atoms can be viewed as a realization of a dynamical Schrödinger cat, because they represent a coherent superposition of two states separated in momentum space, each one corresponding to motion in a classical island of stability.

The evolution in Fig. 5A also shows other interesting transport behavior. There is another oscillation that proceeds more quickly than the tunneling, which appears as population oscillating between the initial peak and the chaotic region near $p = 0$. This can be seen most clearly as an enhanced population near zero momentum during the third, fifth, and seventh modulation periods. This process also points to chaos-assisted tunneling, because it suggests that a third (chaotic) state is involved in the transport between the two islands.

Note added in proof: After the submission of this paper, we became aware of an experiment reporting dynamical tunneling in a similar setting (*35*).

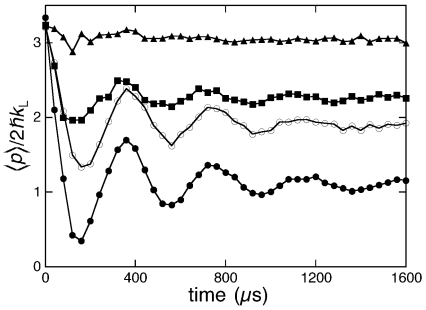

Fig. 3. Comparison of chaos-assisted tunneling for different free-drift times before the standing-wave interaction. The strongest oscillations occur for zero drift time (●), where the initial wave packet is centered on the island of stability as in Fig. 1A. The oscillations are substantially suppressed for a 3.8-μs drift time (■), which displaces the initial wave packet center by 1/4 of a period of the standing wave. Tunneling oscillations are completely suppressed for a 7.6-μs drift time (▲), corresponding to a 1/2-period offset of the initial wave packet. For a 15.1-μs drift time (○), the wave packet is again centered on the island, and coherent oscillations are restored.

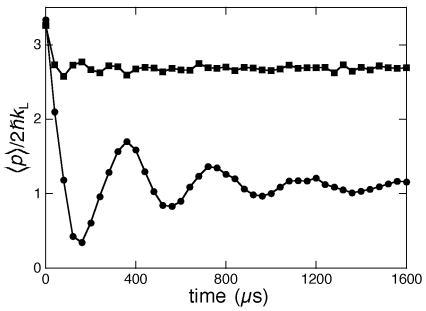

Fig. 4. Comparison of chaos-assisted tunneling oscillations (●) to transport in the corresponding quantum pendulum (■). No tunneling oscillations are observed in the pendulum case over the interaction times studied in the experiment.

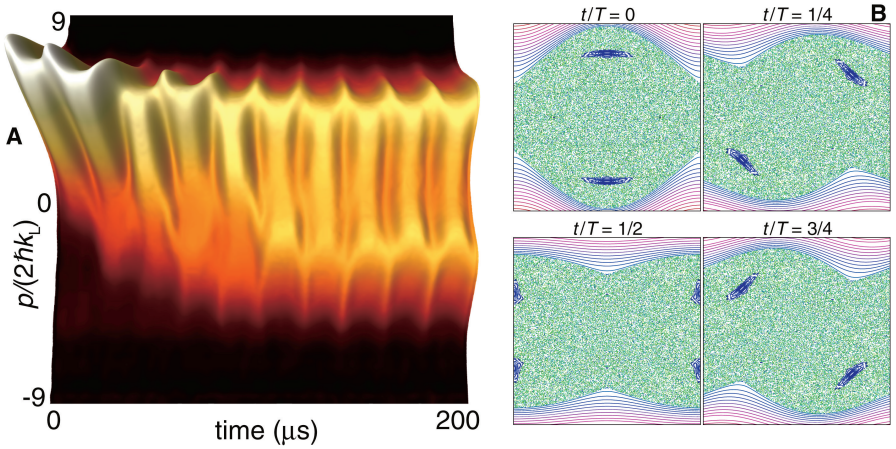

Fig. 5. High temporal resolution tunneling measurement. (**A**) Evolution of the momentum distribution during the first tunneling oscillation, sampled 20 times per modulation period. The two peaks show complementary oscillations at the modulation frequency in addition to the slower tunneling oscillation. Some population also appears in the chaotic region between the islands, especially during the third, fifth, and seventh modulation periods (*34*). (**B**) Phase space plots (axes as in Fig. 1A) at four different phases of the lattice modulation, showing the classical origin of the fast oscillations in (A). At the start of the modulation period, the islands of stability are maximally separated but move inward as they drift away from $x = 0$ and return to their initial momenta by the end of the modulation period. The two islands always remain separated in momentum and do not cross the $p = 0$ axis (*34*).

References and Notes

1. L. E. Reichl, *The Transition to Chaos in Conservative Classical Systems: Quantum Manifestations* (Springer-Verlag, New York, 1992).
2. M. J. Davis, E. J. Heller, *J. Chem. Phys.* **75**, 246 (1981).
3. W. A. Lin, L. E. Ballentine, *Phys. Rev. Lett.* **65**, 2927 (1990).
4. A. Peres, *Phys. Rev. Lett.* **67**, 158 (1991).
5. J. Plata, J. M. Gomez-Llorente, *J. Phys. A* **25**, L303 (1992).
6. R. Utermann, T. Dittrich, P. Hänggi, *Phys. Rev. E* **49**, 273 (1994).
7. O. Bohigas, S. Tomsovic, D. Ullmo, *Phys. Rep.* **223**, 43 (1993).
8. S. Tomsovic, D. Ullmo, *Phys. Rev. E* **50**, 145 (1994).
9. S. D. Frischat, E. Doron, *Phys. Rev. E* **57**, 1421 (1998).
10. A. Mouchet, C. Miniatura, R. Kaiser, B. Grémaud, D. Delande, *Phys. Rev. E*, in press (available at xxx.lanl.gov/abs/nlin.CD/0012013).
11. W. K. Hensinger, A. G. Truscott, B. Upcroft, N. R. Heckenberg, H. Rubinsztein-Dunlop, *J. Opt. B Quant. Semiclass. Opt.* **2**, 659 (2000).
12. M. Hug, G. J. Milburn, *Phys. Rev. A* **63**, 023413 (2001).
13. S. Dyrting, G. J. Milburn, C. A. Holmes, *Phys. Rev. E* **48**, 969 (1993).
14. V. Averbukh, N. Moiseyev, B. Mirbach, H. J. Korsch, *Z. Phys. D* **35**, 247 (1995).
15. C. Dembowski *et al.*, *Phys. Rev. Lett.* **84**, 867 (2000).
16. B. V. Chirikov, D. L. Shepelyansky, *Phys. Rev. Lett.* **74**, 518 (1995).
17. T. Neicu, K. Schaadt, A. Kudrolli, *Phys. Rev. E* **63**, 026206 (2001).
18. P. M. Koch, L. Sirko, R. Blümel, personal communication.
19. D. L. Haycock, P. M. Alsing, I. H. Deutsch, J. Grondalski, P. S. Jessen, *Phys. Rev. Lett.* **85**, 3365 (2000).
20. S. Ghose, P. M. Alsing, I. H. Deutsch, preprint available at xxx.lanl.gov/abs/quant-ph/0102085.
21. R. Graham, M. Schlautmann, P. Zoller, *Phys. Rev. A* **45**, R19 (1992).
22. D. A. Steck, V. Milner, W. H. Oskay, M. G. Raizen, *Phys. Rev. E* **62**, 3461 (2000).
23. J. C. Robinson *et al.*, *Phys. Rev. Lett.* **76**, 3304 (1996).
24. M. T. DePue, C. McCormick, S. L. Winoto, S. Oliver, D. S. Weiss, *Phys. Rev. Lett.* **82**, 2262 (1999).
25. M. A. Kasevich, thesis, Stanford University, Stanford, CA (1992).
26. For an animation of this data (Fig. 1, C and D), see the supplementary material (*36*).
27. P. J. Martin, B. G. Oldaker, A. H. Miklich, D. E. Pritchard, *Phys. Rev. Lett.* **60**, 515 (1988).
28. D. M. Giltner, R. W. McGowan, S. A. Lee, *Phys. Rev. A* **52**, 3966 (1995).
29. M. Kozuma *et al.*, *Phys. Rev. Lett.* **82**, 871 (1999).
30. G. Casati, R. Graham, I. Guarneri, F. M. Izrailev, *Phys. Lett. A* **190**, 159 (1994).
31. S. Tomsovic, *J. Phys. A* **31**, 9469 (1998).
32. For tunneling data with different Raman-selected velocity widths, see the supplementary material (*36*).
33. E. J. Heller, *J. Phys. Chem. A* **103**, 10433 (1999).
34. For animations of the data and phase space in Fig. 5, see the supplementary material (*36*).
35. W. K. Hensinger *et al.*, *Nature*, in press.
36. The supplementary material is available at *Science* Online at www.sciencemag.org/cgi/content/full/1061569.

37. This work was supported by the NSF, the R. A. Welch Foundation, the Sid W. Richardson Foundation, and a Fannie and John Hertz Foundation Fellowship (D.A.S.). D.A.S. acknowledges fruitful discussions with K. W. Madison.

12 April 2001; accepted 1 June 2001
Published online 5 July 2001;
10.1126/science.1061569
Include this information when citing this paper.

Deterministic Delivery of a Single Atom

Stefan Kuhr,* Wolfgang Alt, Dominik Schrader, Martin Müller, Victor Gomer, Dieter Meschede

We report the realization of a deterministic source of single atoms. A standing-wave dipole trap is loaded with one or any desired number of cold cesium atoms from a magneto-optical trap. By controlling the motion of the standing wave, we adiabatically transport the atom with submicrometer precision over macroscopic distances on the order of a centimeter. The displaced atom is observed directly in the dipole trap by fluorescence detection. The trapping field can also be accelerated to eject a single atom into free flight with well-defined velocities.

The manipulation of individual atomic particles is a key factor in the quantum engineering of microscopic systems. These techniques require full control of all physical degrees of freedom with long coherence times. In comparison to well-established single-ion trapping methods (*1–4*), a similar level of control of neutral atoms has yet to be achieved because of their weaker interactions with external electromagnetic fields.

Thermal sources of neutral atoms, such as atomic beams, provide a flux of uncorrelated atoms with random arrival times. However, there is great interest in a source that would deliver a desired number of cold atoms at a time set by the experimentalist. Micromaser experiments, for example, use a dilute atomic beam, which results in a mean number of atoms inside the resonator that is much less than 1. Poissonian statistics, however, dictate that the probability of having more than one atom inside the resonator simultaneously does not vanish; this can easily destroy the ideal one-atom-maser operation (*5*). Another possible application is the controlled generation of single optical photons triggered by atoms entering a resonator with mirrors of ultrahigh reflectivity (a "high-finesse" resonator) one by one (*6, 7*). Other experiments require the placement of more than one atom into the region of interest. Quantum logic gates (*8*) can be implemented by entangling (*2, 4, 9, 10*) neutral atoms through their simultaneous coupling to the optical field of a resonator (*11, 12*). This is possible with the current technology, but in recent experiments (*13, 14*) atoms enter the cavity in a random way, rendering it impossible to have a certain small number of atoms on demand.

In comparison, our technique guarantees control of the position of individual neutral atoms with submicrometer precision. A standing-wave dipole trap is used to store any desired small number of cold atoms in a laser field interference pattern, localizing the trapped atoms to better than half of the optical wavelength. Changing the laser parameters moves this interference pattern along with the trapped atom in a prescribed way. Whereas the transportation of atomic clouds has recently been realized using magnetic potentials (*15*), here we demonstrate the controlled transport of a single atom.

Optical dipole traps (*16–21*) are based on the interaction between an electric component of the light field $\mathbf{E}$ and the induced atomic electric dipole moment $\mathbf{d}$, which is proportional to $\mathbf{E}$. The interaction energy $U = -\langle \mathbf{d} \cdot \mathbf{E} \rangle/2$ is proportional to the local light intensity. If the laser frequency is smaller than the atomic resonance frequency, the atom is attracted to the region of maximum intensity. Thus, the simplest optical dipole trap is a focused laser beam. Tuning the laser frequency far away from all atomic resonances substantially reduces the photon scattering rate, and the atom is trapped in a nearly conservative potential. In contrast, a magneto-optical trap (MOT) (*22*) provides dissipative forces and serves as a convenient source of single cold atoms (*23, 24*). Atoms captured from the background gas interact with the near-resonant light field of the MOT and scatter photons from the laser beams. This fluorescence signal monitors the number of trapped atoms in real time (Fig. 1). These atoms can be transferred into a dipole trap superimposed on the MOT without any loss, thus allowing us to experiment with a predetermined number of atoms (*24*).

Our dipole trap consists of two counterpropagating laser beams with equal intensities and optical frequencies ν_1 and ν_2, producing a position-dependent dipole potential $U(z, t) = U_0 \cos^2[\pi(\Delta\nu t - 2z/\lambda)]$, where U_0 is the local trap depth, z is the position of the atoms, $\lambda = 1064$ nm is the optical wavelength ($\lambda = c/\nu_1 \approx c/\nu_2$, where

Institut für Angewandte Physik, Universität Bonn, Wegelerstrasse 8, D-53115 Bonn, Germany.

*To whom correspondence should be addressed. E-mail: kuhr@iap.uni-bonn.de